Brodogradnja/Shipbilding/Open access Volume 74 Number 3, 2023

Haoyun Tang
Qian Wan
Huilong Ren

http://dx.doi.org/10.21278/brod74306

ISSN 0007-215X
eISSN 1845-5859

Numerical study of trimaran wave load based on time-domain Rankine method

UDC 629.5.022.3:621.3.016.3
Original scientific paper

Summary

Due to the complex fluid interference between outrigger and main hull, it is difficult to predict the trimaran load fluctuation accurately in different marine environments. Therefore, a time-domain Rankine method is developed to improve the accuracy of trimaran load prediction. This method successfully adds the nonlinear load components in time-domain load simulation by taking into account the factors such as instantaneous hull wetted surface, steady ship waves, green wave and slamming. Additionally, the nonlinear growth of green wave and slamming is also observed at outrigger and wet deck, with the increasing of speeds and wave heights. Finally, the relatively smaller errors in the Rankine method are confirmed by comparison with the values from a trimaran model test and linear time-domain load prediction method. Furthermore, the weakly nonlinear Rankine method is considered to be more suitable for trimaran load prediction under harsh marine environment.

Key words: trimaran; potential flow theory; Rankine method; wave load

1. Introduction

Trimaran has always attracted a great deal of attention across the international shipbuilding industry, due to its multiple advantages such as high speed, spacious platforms and excellent seakeeping performance [1]. The high-speed trimaran has thus become one of the main representatives of high-performance multihulls. However, while the unique trimaran structure offers multiple favourable fluid interferences, it also increases the complexity of fluid field fluctuation around trimarans. Therefore, it is necessary to provide a load prediction method to simulate the trimaran load fluctuation accurately in complex marine environment.

For ship load simulation in various wave scenarios, potential flow theory is often applied. In the potential flow theory, some potential functions are established to describe the interaction between waves and ships [2,3]. In order to solve these potential functions, a kind of boundary element method, which is based on Rankine source, is widely used in trimaran load simulation [4-6]. Many experts had carried out a series of meaningful researches and achieved valuable results using the Rankine method. Shin developed a program by Rankine

method to predict ship motion and load [7]. In his research, the Rankine model was applied with an artificial damping beach and some simplified calculations of green water. This program then successfully predicted the trimaran load fluctuation in seas. Subsequently, in Xiang and Xu's research [8,9], the Rankine methods were extended to simulate the ship load in irregular waves. The characteristics of trimaran load fluctuation in different wave cases was also illustrated. Deng then developed a time-domain three-dimensional Rankine method to analyse the influence of different dimensions on trimaran load [10]. In order to reduces the computational cost, Tang also developed a numerical method by combining Rankine with free surface Green functions [11]. Under the artificial free surface truncation domain, this method included the speed effect on trimaran load, to a certain extent. Additionally, Khoob combined the Rankine method with Finite element method to achieve the short-term prediction of a wave-piercing trimaran load [12]. Although theoretical prediction of trimaran load using the time-domain Rankine method had gained fruitful achievements, there were still some errors in the theoretical prediction of large-scale trimarans, especially under the conditions of large wave heights and high speeds. The previous researches mainly focused on unsteady wave disturbance, which ignored the interaction between steady ship waves and unsteady fluid field disturbances. The steady ship waves towards trimaran are obvious, when the trimaran is sailing at high speed. These steady ship waves would affect the fluctuation of hull wetted surfaces and instantaneous wave impacts. In fact, due to the mutual disturbance between outrigger and main hull, the trimaran load fluctuation is more complex than that of monohulls. Furthermore, the instantaneous phenomena of green water and slamming at the bows of the main hull and outriggers cannot be neglected, which result in the inevitable nonlinear impact during the trimaran navigation. Relevant experimental researches show that these nonlinear load components were potentially dangerous for trimaran long-term navigation [13-15]. Thus, a time-domain nonlinear Rankine method is required to assist with trimaran structural design.

This paper focuses on the numerical simulation of wave-induced loads on trimarans, particularly with regard to nonlinear load components. In order to achieve this goal, various nonlinear factors, such as steady ship waves, instantaneous hull wetted surface, slamming, and green water, are included into the whole simulation process. The solution of steady ship waves is based on fully nonlinear free surface condition. The influence of the steady ship waves is then taken into account in the calculation of unsteady flow field disturbances. The unsteady velocity potential simulation also covers the influence of body surface nonlinearity caused by ship significant motion. Furthermore, the phenomena of green water and slamming are further simulated to bring the instantaneous wave impact into the trimaran load. Some comparative analyses with varied panel density conditions on free surfaces and body surfaces are undertaken to verify the stability of the nonlinear Rankine method. The values of the relevant panel parameters determined in these analyses are recommended for general engineering application. Finally, the load forecasting results from the nonlinear Rankine method were compared with the results from traditional linear potential flow methods and model tests. The reliability of the nonlinear Rankine method for trimaran load is proved. Considering its excellent numerical stability and relatively high prediction accuracy, this Rankine method can contribute to the structural optimisation of trimaran design.

2. Mathematical model for the interaction between ships and waves

2.1 Establishment of velocity potentials in waves

In potential flow theory, the assumption of ideal fluid is applied. The flow around a ship is regarded as an incompressible and inviscid fluid with surface tension ignored, and the fluid flow is also assumed to be irrotational. When the ship is sailing at a steady forward speed U, three right-hand coordinate systems are built: i) a space-fixed system O_0-$x_0y_0z_0$ with its origin

O_0 at still water; ii) an inertial reference system *O-xyz* is located at the mean free surface and moving with uniform speed *U*; and iii) a hull-fixed system *G-x´y´z´* is fixed at the ship centre of gravity. A series of velocity potential functions thus exist to describe the fluctuation of the fluid field. In the inertial reference coordinate, the velocity potential can be decomposed as follow:

$$\Psi = -Ux + \Phi + \psi(t) \tag{1}$$

where (*-Ux*) denotes the uniform flow potential; Φ is the steady basic velocity potential; ψ is the unsteady velocity potential. *t* is the time in numerical simulation. In order to effectively describe these velocity potentials, some boundaries are constructed in the ideal fluid field, as shown in Fig.1. Herein, S_∞ denotes the infinity boundary of the fluid field; S_F denotes the free surface of the wave environment. S_B denotes the hull wetted surface, and it is the interface between hull shells and waters.

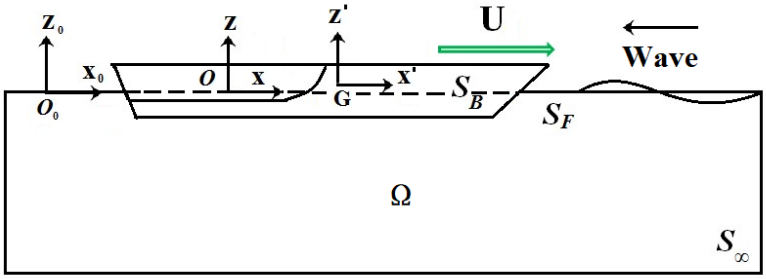

Fig.1 Boundaries of the ideal fluid field

In order to illustrate the fluctuation of free surface, the free surface fluctuation also consists of three elevation parts in the simulation:

$$\zeta(t) = \zeta_I(t) + \zeta_S(t) + \zeta_D(t) \tag{2}$$

where ζ_I denotes the incident wave elevation; ζ_S denotes the steady wave elevation, which is caused by steady ship waves. ζ_D denotes the unsteady wave elevation, and it is the result of unsteady velocity potential on fluid field disturbance.

2.2 Solution of steady basic velocity potential

According to the characteristics of the fluid field on these boundaries, the boundary value problems for these velocity potentials are established. The steady basic velocity potential Φ follows the Laplace equation in the ideal fluid, and its boundary value problems can be expressed as:

$$\begin{cases} \nabla^2\Phi = 0 & ;in \quad Fluid \\ \dfrac{\partial\Phi}{\partial n} = U\cdot\vec{n} & ;on \quad S_B \\ (-U + \dfrac{\partial\Phi}{\partial x})\dfrac{\partial\zeta_s}{\partial x} + \dfrac{\partial\Phi}{\partial y}\dfrac{\partial\zeta_s}{\partial y} - \dfrac{\partial\Phi}{\partial z} = 0 & ;on \quad S_F \\ -U\dfrac{\partial\Phi}{\partial x} + \dfrac{1}{2}\nabla\Phi\cdot\nabla\Phi + g\zeta_s = 0 & ;on \quad S_F \\ \Phi = O(\dfrac{1}{\sqrt{x^2+y^2}}) & ;on \quad S_\infty \end{cases} \tag{3}$$

where $\vec{n}$ is the unit normal vector at hull surfaces; g is the acceleration of gravity. Because the dynamics and kinematics free surface conditions in the ideal fluid have nonlinear characteristics, these free surface conditions are difficult to be directly solved [16]. Therefore, the basic velocity potential in the nonlinear free surface condition is approximated by iterative calculation. The iterative solution is divided into two stages. Initially, the linearized free surface condition without consideration of wave fluctuation is used to find the initial value for an iterative calculation, as shown in Eq. (4). Then, the iterative scheme offered in Eq. (5) is further applied to find the final basic velocity potential.

$$\frac{U^2}{g}\frac{\partial^2\Phi}{\partial x^2}+\frac{\partial\Phi}{\partial z}=0 \qquad ;on \quad S_F \tag{4}$$

$$\begin{aligned}&\Phi_z^l+\frac{U}{g}\left[U\Phi_{x,x}^l-\Phi_x^{l-1}\Phi_{x,x}^{l-1}-\Phi_y^{l-1}\Phi_{y,x}^{l-1}-\Phi_z^{l-1}\Phi_{z,x}^{l-1}\right]-\frac{1}{g}\left[U\Phi_x^{l-1}\Phi_{x,x}^{l-1}-\Phi_x^{l-1}\Phi_y^{l-1}\Phi_{y,x}^{l-1}-\Phi_x^{l-1}\Phi_z^{l-1}\Phi_{z,x}^{l-1}\right]\\&-\frac{1}{g}\left[U\Phi_y^{l-1}\Phi_{x,y}^{l-1}-\Phi_y^{l-1}\Phi_x^{l-1}\Phi_{x,y}^{l-1}-\Phi_y^{l-1}\Phi_z^{l-1}\Phi_{z,y}^{l-1}\right]-\frac{1}{g}\left[-\Phi_x^{l-1}\Phi_x^{l-1}\Phi_{x,x}^{l-1}-\Phi_x^{l-1}\Phi_y^{l-1}\Phi_{y,y}^{l-1}\right]=0\end{aligned} \tag{5}$$

where l is the current step of the iterative calculation. In order to facilitate the formula expression, the signs about the first and second order partial derivatives of basic velocity potential are simplified in Eq. (5). Herein, the superscript of basic velocity potential uses as the iterative step number in the calculation, and its subscript denotes the numerical derivation direction. In this iterative calculation, the free surface elevation caused by steady ship waves is an important parameter for the termination condition, as seen in Eq. (6). When the residual error of the steady wave elevation calculation is lower than 10^{-6}, the calculated basic velocity potential is regarded as the final stable value. In general, the calculation of basic velocity potential for a trimaran often converges at the 50th iterative step.

$$\zeta_S=\frac{1}{g}\left(U\frac{\partial\Phi}{\partial x}-\frac{1}{2}\nabla\Phi\cdot\nabla\Phi\right) \tag{6}$$

2.3 Solution of unsteady basic velocity potential

According to the characteristics of unsteady fluid disturbance, the unsteady velocity potential can be further decomposed into the following format:

$$\psi(t)=\phi(t)+\varphi(t) \tag{7}$$

where $\phi(t)$ denotes unsteady local velocity potential; and $\varphi(t)$ denotes unsteady memory velocity potential. The velocity potential decomposition method is based on the Kring's research [17]. Wang and Li follow this velocity potential decomposition and also obtained relatively satisfactory results [18,19]. Although the velocity potential decomposition form is different with the traditional decomposition method, the essence of this decomposition is the same. In fact, one part of radiation potential is separated into this local potential, and the other part is attributed to the memory potential. The diffraction potential is fully included in the memory potential. The local velocity potential represents the instantaneous effect of hull motion on the surrounding fluid, and its extraction can improve the stability of numerical simulation.

After the steady basic velocity potential is obtained, the boundary value problems for the local velocity potential ϕ(t) can be established by considering the ship motion in waves. Eq. (8) shows the boundary conditions satisfied by the local velocity potential in the ideal fluid:

$$\begin{cases} \nabla^2\phi=0 & ;in \quad Fluid \\ \phi=0 & ;on \quad S_F \\ \dfrac{\partial\phi}{\partial n}=\sum_{k=1}^{6}\left(\dot{\eta}_k(t)n_k+\eta_k(t)m_k\right) & ;on \quad \bar{S}_B \end{cases} \tag{8}$$

herein, η_j is the hull motion at moment *t*. m_j and n_j denote the fluid coupling disturbance term and hull normal vector term:

$$\begin{cases} (n_1,n_2,n_3)=\vec{n} \\ (n_4,n_5,n_6)=\vec{r}\times\vec{n} \end{cases} \tag{9}$$

$$\begin{cases} (m_1,m_2,m_3)=\left(\vec{n}\cdot\nabla\right)\left(U-\nabla\Phi\right) \\ (m_4,m_5,m_6)=\left(\vec{n}\cdot\nabla\right)\left[\vec{r}\times\left(U-\nabla\Phi\right)\right] \end{cases} \tag{10}$$

where $\vec{r}$ is the position vector based on the coordinate origin. The chain rule [20] is applied to calculate second-order spatial partial derivative of steady velocity potentials and the fluid coupling disturbance term. In fact, the terms (m_4,m_5,m_6) can also be obtained by the functional relationship of the terms (m_1,m_2,m_3):

$$\begin{cases} m_4=(m_3y-m_2z)+\left(\dfrac{\partial\Phi}{\partial y}n_3-\dfrac{\partial\Phi}{\partial z}n_2\right) \\ m_5=(m_1z-m_3x)+\left[\dfrac{\partial\Phi}{\partial z}n_1-\left(\dfrac{\partial\Phi}{\partial x}-U\right)n_3\right] \\ m_6=(m_2x-m_1y)+\left[-\dfrac{\partial\Phi}{\partial y}n_1+\left(\dfrac{\partial\Phi}{\partial x}-U\right)n_2\right] \end{cases} \tag{11}$$

Considering the ship motion in six degrees of freedom, the unsteady local velocity potential can be further divided into the normalized velocity potentials:

$$\phi=\sum_{k=1}^{6}\phi_k=\sum_{k=1}^{6}\left[N_k\dot{\eta}_k(t)+M_k\eta_k(t)\right] \qquad (k=1,2,3\cdots,6) \tag{12}$$

Thus, combining Eq. (8) with Eq. (12), the normalized boundary value problems for the normalized velocity potentials (N_j and M_j) are obtained:

$$\begin{cases} N_k=M_k=0 & ;on \quad S_F \\ \dfrac{\partial N_k}{\partial n}=n_k,\dfrac{\partial M_k}{\partial n}=m_k\ (k=1,2,3\cdots,6) & ;on \quad \bar{S}_B \end{cases} \tag{13}$$

The local velocity potential can be finally solved by using the Rankine source introduced in Section 2.2. The body boundary condition of the unsteady velocity potential is derived by perturbation expansion on the interface between hull shells and waters, and it is also satisfied on mean wetted body surface [21]. Although the instantaneous wetted body surface is varied with time in the actual wave environment, the mean wetted body surface is a constant and applied in most engineering calculations. The mean wetted body surface is usually obtained at the calm water condition. The calculation of unsteady velocity potential at the mean wetted body surface is relatively stable and fast. But the invariant mean wetted body surface ignores the influence of body surface nonlinearity caused by ship significant motion. Therefore, a mean instantaneous hull wetted surface $\bar{S}_B(t)$ was constructed to make the mean wetted body surface change with ship motion [22]. The mean instantaneous hull wetted

surface is a varied mean wetted body surface, which is calculated by considering the real-time change of relative position between ship and mean free surface. In the mean instantaneous hull wetted surface, the wetted body surface will be updated at each time step. The calculation of hydrodynamic coefficients and hydrodynamic forces are then taken at the new wetted body surface. Due to the fact that the mean instantaneous hull wetted surface still belongs to the category of the mean wetted body surface, the linear boundary condition for unsteady velocity potential can be still used in the solution process. But the integration interval in solving hydrodynamic forces are time variables, which are different from the traditional potential flow theory. According to the Bernoulli equation, the hydrodynamic forces caused by the local velocity potential are obtained:

$$F_L = -\rho \iint_{\bar{S}_B(t)} (p_L \cdot \vec{n}) ds = -\sum_{k=1}^{6} \left[a_{jk} \ddot{\eta}_j(t) + b_{jk} \dot{\eta}_j(t) + c_{jk} \eta_j(t) \right] \tag{14}$$

where p_L is hydrodynamic pressure caused by the local velocity potential. Since the local velocity potential is related to the ship motion, the hydrodynamic force can also be expressed by the hydrodynamic coefficients and ship motion. These hydrodynamic coefficients are respectively expressed as:

$$a_{jk} = \rho \iint_{\bar{S}_B(t)} N_k \cdot n_j \mathrm{d}s \tag{15}$$

$$b_{jk} = \rho \iint_{\bar{S}_B(t)} \left[M_k - (U - \nabla\Phi) \nabla N_k \right] n_j \mathrm{d}s \tag{16}$$

$$c_{jk} = \rho \iint_{\bar{S}_B(t)} \left[-(U - \nabla\Phi) \nabla M_k \right] n_j \mathrm{d}s \tag{17}$$

According to the characteristics of different numerical solutions, the memory velocity potential is also decomposed into two parts: a memory part χ_k and a diffraction part φ_7. In the solution of memory velocity potential, the linearized free surface boundary conditions are applied to improve the stability of the numerical simulation. The boundary conditions for memory part are obtained:

$$\begin{cases} \nabla^2 \chi_k = 0 & ;in \quad Fluid \\ \left[\left(\dfrac{\partial}{\partial t} - U \dfrac{\partial}{\partial x} \right)^2 + g \dfrac{\partial}{\partial z} \right] \left(\chi_k + M_k \right) = 0 & ;on \quad S_F \\ \chi_k \big|_{t=0} = 0, \quad \left. \dfrac{\partial \chi_k}{\partial t} \right|_{t=0} = -g \dfrac{\partial N_k}{\partial z} & ;on \quad S_F \\ \dfrac{\partial \chi_k}{\partial n} = 0 & ;on \quad \bar{S}_B \end{cases} \tag{18}$$

The memory part χ_k is calculated by combining the numerical results of local velocity potential (M_k and N_k). Herein, the calculation of waterline integral term follows the Liapis' research [23]. The wave memory effect is described by a special function, which is called the memory function. This memory function is expressed as:

$$K_{jk} = \rho \iint_{\bar{S}_B(t)} \left(\frac{\partial \chi_k}{\partial t} n_j - \chi_k m_j \right) \mathrm{d}s \tag{19}$$

Fig.2 shows the calculation results of memory functions for a trimaran. The dimensionless heave and pitch functions ($K'_{33} = (K_{33}L)/(\rho\nabla g); K'_{55} = K_{55}/(\rho\nabla g)$) are applied.

The speed effect and the outrigger fluid interference may lead to some prolonged fluctuations. The similar fluctuations are also found in Sun and Tang's research [24,25].

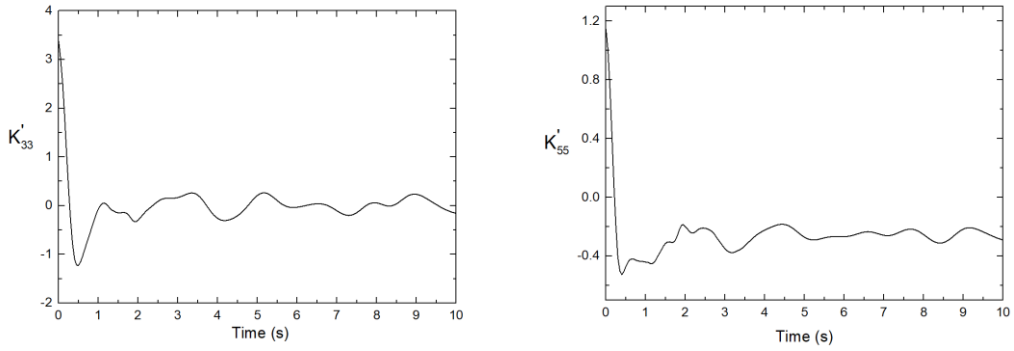

(a) (b)

Fig.2 Calculation results of dimensionless memory functions (*H*=1.0m, *U*=8kn, $\lambda / L = 1.0$): (a) dimensionless heave function; (b) dimensionless pitch function

The boundary conditions for diffraction part φ_7 are also established:

$$\begin{cases} \nabla^2 \varphi_7 = 0 & ;in \quad Fluid \\ \left(\dfrac{\partial}{\partial t} - U \dfrac{\partial}{\partial x} \right)^2 \varphi_7 + g \dfrac{\partial \varphi_7}{\partial z} = 0 & ;on \quad S_F \\ \varphi_7 \big|_{t=0} = \left. \dfrac{\partial \varphi_7}{\partial t} \right|_{t=0} = 0 & ;on \quad S_F \\ \dfrac{\partial \varphi_7}{\partial n} = -\dfrac{\partial \varphi_I}{\partial n} & ;on \quad \bar{S}_B \end{cases} \tag{20}$$

where φ_I denotes the incident wave potential. The formula of the incident wave potential and its wave surface elevation are expressed as:

$$\varphi_I(t) = \frac{H_a g}{\omega} e^{kz} \sin\left[k_I (x\cos\beta + y\sin\beta) - \omega t + \varepsilon\right] \tag{21}$$

$$\zeta_I(t) = H_a \cos\left[k_I (x\cos\beta + y\sin\beta) - \omega t + \varepsilon\right] \tag{22}$$

where β is the heading angle for wave propagation; ω is the fluctuation frequency of simulated regular waves. H_a is the simulated wave amplitude; ε and k_I denotes the wave phase and the wave number, respectively. An impulse response function $\hat{\varphi}_7$ is applied to solve the diffraction potential and the diffraction force:

$$\varphi_7 = \int_{-\infty}^{\infty} \hat{\varphi}_7 (t-\tau) \zeta_I(\tau) \mathrm{d}\tau \tag{23}$$

$$F_D(t) = -\rho \int_{-\infty}^{\infty} \zeta_I(\tau) \mathrm{d}\tau \iint_{\bar{S}_B(t)} \left[\frac{\partial \hat{\varphi}_7 (t-\tau)}{\partial t} n_j - \hat{\varphi}_7(t) m_j \right] \mathrm{d}s \tag{24}$$

The diffraction potential and the diffraction force are finally obtained by using the impulse response function method, according to the Kring's research [17]. The memory velocity potential is finally calculated by combining the basic velocity potential and the local velocity potential. In fact, on the body surface, the interaction between unsteady flow and steady flow is added by the application of the m_j term. This interaction at free surface cannot be included directly, due to the linearized free surface boundary conditions. By frequently calculating the relative position of ship to the mean free surface (z=0) which is equilibrium

position for the perturbation expansion, the mean instantaneous hull wetted surface $\bar{S}_B(t)$ is updated in the time domain solution. In the update calculation, the mean free surface position (z=0) remains unchanged, and the ship position changes by the real-time calculated motion and floating condition. This numerical update method can cover the body surface nonlinearity caused by ship significant motion in an indirect way, which is also called weakly nonlinear solution method for unsteady velocity potential.

2.4 Rankine source and Green function method

In order to simulate the interaction between ships and waves, it is essential to establish the boundary integral equation and provide a stable solution. According to the characteristics of boundary conditions, the calculation of local velocity potential belongs to the traditional boundary value problem, while the memory velocity potential solution is a type of mixed initial-boundary value problem. The Green function method is applied to solve the boundary value problems. According to Green's second theorem, the integral equation at the fluid field boundaries can be expressed as:

$$C(p)\psi(p)=\int_S\left[G(p,q)\frac{\partial}{\partial n_q}\psi(q)-\psi(q)\frac{\partial}{\partial n_q}G(p,q)\right]ds_q \tag{25}$$

where p and q denote the field point and source point, respectively. $C(p)$ is the solid angle coefficient at field point p, and its value is related to the spatial position:

$$C(p)=\begin{cases}1 & ;\text{In fluid domain}\\ 4\pi & ;\text{Fluid boundary}\\ 2\pi & ;p\to q\\ 0 & ;\text{other situations}\end{cases} \tag{26}$$

Under the infinite water depth condition, the Rankine source is selected as the Green function:

$$G(p,q)=\frac{1}{r} \tag{27}$$

where r is the relative distance between field point and source point. In the numerical solution, the boundary integral equation is discretised into several small panels at the boundary and solved using the panel method [26]. The velocity potentials and related hydrodynamic forces are finally obtained using this Green function method.

2.5 Damping layer and filtering at free surface

In time-domain simulation, the velocity potential is regarded as the function with time fluctuation. The time stepping algorithm is thus used to solve the free surface condition of the velocity potential. In the time stepping algorithm, the fluctuation of velocity potential and wave surface around ships are further described by the fourth Runge-Kutta model. Additionally, in order to improve the numerical stability of interaction between waves and ships, some critical numerical processing methods are applied at each time step. In fact, because the Rankine source lacks the automatic satisfaction of infinity free surface radiation condition, a reasonable truncated calculation domain is required in the numerical free surface. Therefore, it is necessary to build a numerical coast and apply the wave absorbing principle to deal with the wave radiation problem [20]. In the specific calculation process, the damping coefficient μ_0 is added into the kinematic free surface condition $H(\psi,\zeta,t)$ and the dynamic free surface condition $L(\psi,\zeta,t)$, as follows:

$$\frac{\partial \zeta}{\partial t} = H(\psi, \zeta, t) - \mu_0 (\frac{\gamma}{R})^2 \zeta \tag{28}$$

$$\frac{\partial \psi}{\partial t} = L(\psi, \zeta, t) - \mu_0 (\frac{\gamma}{R})^2 \psi \tag{29}$$

where R denotes the range size of the damping layer, and γ is the distance between the calculation point at the free surface and the base point on the damping layer. The establishment of the damping layer in numerical coast helps avoid interference from wave reflections in the calculation domain of the free surface. In addition to radiation wave reflection problem, some unstable short waves in the numerical solution may also result in computational divergence. Longuet-Higgins' research indicated that unstable numerical short waves often appear when the time-domain boundary element method is applied to calculate fluctuations of the free surface, especially in sailing speed cases [27]. Thus, a low-pass filter with multiple nodes in the free surface is also applied to filter the fluctuating short wave. The following is the numerical filter design after applying the wave filtering principle:

$$\zeta_i^1 = \zeta_i^0 + \varepsilon_w (\zeta_{i+1}^0 + \zeta_{i-1}^0 - 2\zeta_i^0) \tag{30}$$

where i is the node identifier along the ship length or breadth at the free surface; ζ_i^0 denotes the node height before filtering; ζ_i^1 denotes the node height after filtering; and ε_w is the filter coefficient.

2.6 Motion and load simulation for a trimaran

In the potential flow theory, the fluid field around trimaran can be described by some calculated velocity potentials. According to Newton's second law, the differential equation for trimaran motion in waves can be expressed as:

$$M_{ij} \ddot{\eta}_j(t) = F(t) \tag{31}$$

where M_{ij} is the generalised mass matrix, and $F(t)$ denotes the fluid force. Taking the characteristics of trimaran load into account, this fluid force is decomposed as:

$$F(t) = F_W(t) + F_L(t) + F_D(t) + \int_0^t K_{jk}(t-\tau)\dot{\eta}_j(\tau)\,\mathrm{d}\tau + F_{slam}(t) + F_{gw}(t) \tag{32}$$

where $F_{slam}(t)$ denotes the slamming force; $F_{gw}(t)$ denotes the green water force; $F_L(t)$ denotes the local fluid force; K_{jk} is the memory function; $F_D(t)$ denotes the diffraction force; $F_W(t)$ is the nonlinear wave exciting force and it is calculated by the wave surface pressure correction method [28]. When the incident wave surface rises $(\zeta_I > 0)$, the condition that water pressure at the wave surface $(z = \zeta_I)$ is zero is easily satisfied. The wave pressure can be expressed as:

$$p_{W-R}(t) = \begin{cases} \rho g \zeta_I(t) - \rho g z & [0 \le z \le \zeta_I(t)] \\ \rho g \zeta_I(t) \cdot e^{k_I z} - \rho g z & (z < 0) \end{cases} \tag{33}$$

when the incident wave surface falls $(\zeta_I < 0)$, the pressure at wave trough needs to be further modified, according to the same wave surface condition. The wave pressure can be finally expressed as:

$$p_{W-F}(t) = \begin{cases} 0 & [\zeta_I(t) \le z \le 0] \\ \rho g \zeta_I(t) \cdot e^{kz} - \rho g z & (z \le \zeta_I) \end{cases} \tag{34}$$

Herein, this wave pressure includes the incident wave pressure and the hydrostatic pressure. The calculation formula of wave pressure is then unified. The nonlinear wave exciting force is obtained by integrating the wave pressure p_W on an instantaneous wetted body surface $\tilde{S}_B(t)$ and subtracting the integral result of the initial hydrostatic pressure p_0 at the wetted body equilibrium position of calm water condition:

$$F_W(t)=\begin{cases}\iint\limits_{\tilde{S}_B(t)}\left[\rho g\zeta_I(t)-\rho gz\right]n_j ds-\iint\limits_{S_B}p_0 n_j \mathrm{d}s & (0\le z\le\zeta_I)\\ \iint\limits_{\tilde{S}_B(t)}\left[\rho g\zeta_I(t)\cdot e^{k_I z}-\rho gz\right]n_j ds-\iint\limits_{S_B}p_0 n_j \mathrm{d}s & (z<\min[0,\zeta_I])\end{cases} \tag{35}$$

Because the hydrostatic restoring force is the difference between the ship gravity and the total hydrostatic pressure when ship leaves its initial equilibrium position. The wave exciting force includes the incident wave force and the hydrostatic restoring force. In addition, due to the wave exciting force is calculated at the instantaneous wetted body surface. This force is no longer harmonic and can catch the influence of body surface nonlinearity more convenient.

In the simulation of hydrodynamic forces, the nonlinear instantaneous impacts such as green water and slamming are included. The green water force is simulated using the numerical model of flood waves, according to Buchner's research [29]. The simplified calculation model for green water force is shown in Eq. (36), which is applicable when wave relative height ζ_w is higher than the ship freeboard H_{fb}. According to the momentum theorem based von Karman model [30,31], slamming force can also be simulated as shown in Eq. (37). In the wave slamming simulation, the slamming force only appears in conditions whereby the hull vertical relative velocity V_3 is less than zero.

$$F_{gw}(t)=\begin{cases}\int\left\{\dfrac{d\left[\rho\dot{Z}_d(\tilde{x})h_{gw}(\tilde{x},t)\right]}{dt}+\rho g h_{gw}(\tilde{x},t)\cos\eta_5(t)\right\}dx; & \zeta_w>H_{fb}\\ 0 \quad ; & \zeta_w\le H_{fb}\end{cases} \tag{36}$$

$$F_{slam}(t)=\begin{cases}\int\left\{\dfrac{dm_\infty(\tilde{x})}{dz}[\dfrac{d}{dt}(\eta_3(t)-\tilde{x}_b\eta_5(t)-\zeta_w(t))]^2\right\}dx; & V_3(\tilde{x})<0\\ 0 \quad ; & V_3(\tilde{x})\ge 0\end{cases} \tag{37}$$

where $\tilde{x}$ is the longitudinal position for green water and wave slamming; Z_d is the vertical displacement of the bow deck by ship heave and pitch, when green water phenomena occur. h_{gw} denotes the relative green water height over the freeboard, which contains the incident wave fluctuation and the wave surface elevation caused by unsteady fluid disturbance and steady ship waves. m_∞ is the additional mass term when the encounter frequency tends to infinity; $\tilde{x}_b$ is the longitudinal distance from the ship's gravity centre; ζ_w is relative wave height around the ship, which is also combination of incident wave fluctuation, unsteady fluid disturbance and steady ship waves. Due to the varied occurrence positions of green water phenomena, the trimaran green water force is further divided into two parts, which are green water impact at the outrigger bow and at the main hull bow. Similarly, the slamming force on the trimaran consists of the main hull bow slamming, the outrigger bow slamming and the wet deck slamming. Herein, the wet deck slamming includes the wave impact forces at lower deck of cross-bridge and internal hull shell of tunnel. The green wave and slamming forces are calculated respectively and imposed on the trimaran shell, according to the different wave

impact positions. Finally, the trimaran motion equation, which takes instantaneous impacts into account, is achieved as follows:

$$(M+a)\ddot{\eta}_j(t)+b\dot{\eta}_j+\int_0^t K(t-\tau)\dot{\eta}_j(\tau)\mathrm{d}\tau+c\eta_j=F_W(t)+F_{slam}(t)+F_{gw}(t) \quad (38)$$

The fourth-order Runge Kutta method is used to solve this differential equation. In the time-domain simulation, due to rapid changes from the quiescent state to the speed condition, the simulated hydrodynamic force and ship motion may appear large oscillations at initial. Therefore, a smoothing function is applied at the beginning of hydrodynamic force simulation to allow trimaran motion to be gradually affected by external fluid forces in the whole calculation process:

$$SM(\sigma)=\frac{1}{2}\left[1-\cos(\frac{\pi\xi}{\sigma})\right] \qquad (\xi=1,2,\cdots,\sigma) \quad (39)$$

where ξ is the applied number of smoothing functions for the current simulation, and σ is the total number of smoothing functions. In the simulation of hydrodynamic forces, the smoothing function lasts 11.5s. Furthermore, wave-induced loads are obtained by combining the inertia forces of ship motions with the fluid hydrodynamic pressures:

$$M_v(\tilde{x},t)=\int_{V(x)} a_m dm-\int_{S(x)} p_F n_j ds \qquad (j=1,2,...,6) \quad (40)$$

where $M_v(\tilde{x},t)$ denotes the wave-induced load at the longitudinal position $\tilde{x}$. a_m and p_F are the mass acceleration and the fluid hydrodynamic pressure, respectively. Fig.3 shows a basic sketch for the whole numerical simulation.

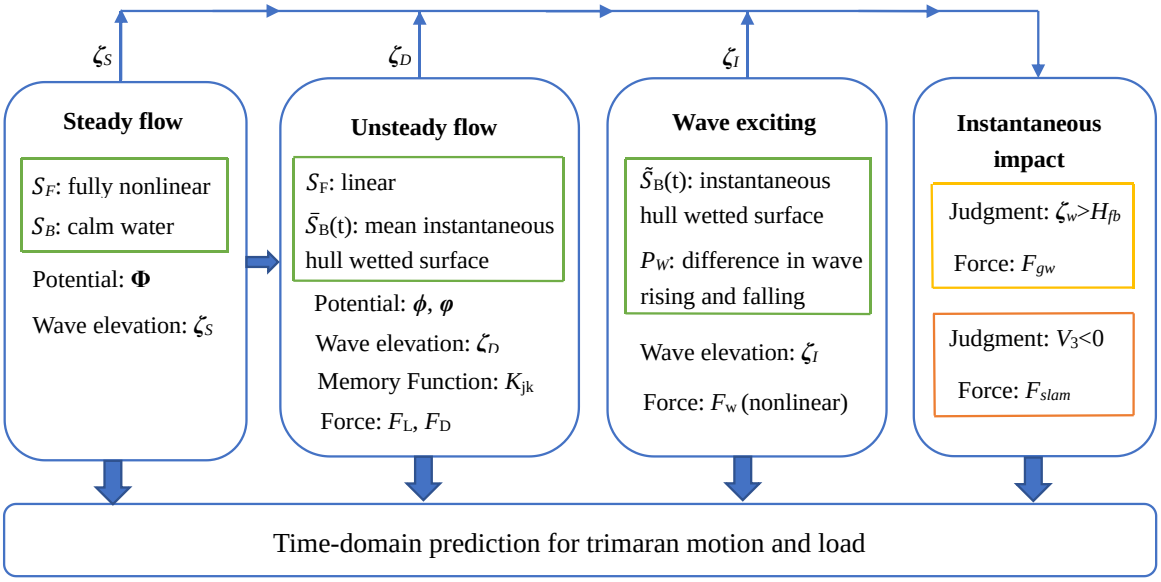

Fig.3 Sketch of theoretical prediction for trimaran motion and load

3. Results and discussions

3.1 Hydrodynamic panel generation in the simulation

A large-scale trimaran is used for numerical simulation and analysis in this paper, as shown in Fig.4. The selected trimaran dimensions (length, width and depth) are 141 m, 27 m and 13m. The trimaran draft is 6 m. There is a design of bulbous bow and square stern on this trimaran arrangement.

Fig.4 Three-dimensional design of trimaran

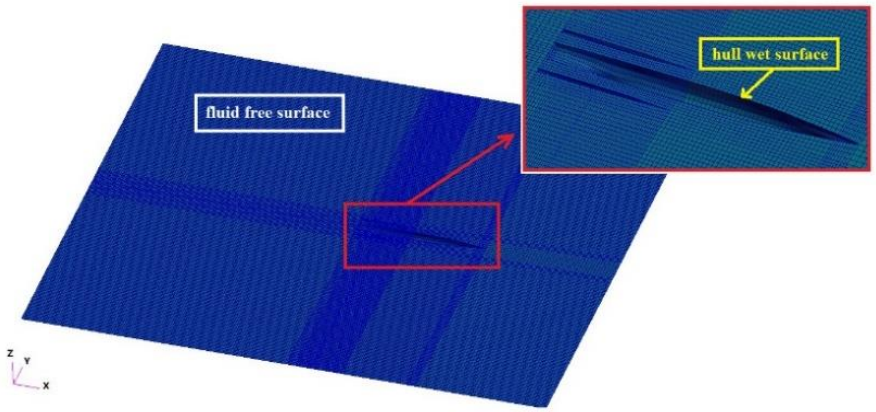

Fig.5 Hydrodynamic panel for trimaran simulation

Fig.5 shows the hydrodynamic panel generation in the numerical simulation. For the fluid free surface simulation, a numerical rectangular surface is taken, which is convenient to calculate the spatial derivative of velocity potentials by using the second-order upwind difference method. The panels in the free surface always belong to the quadrilateral panel type and are arranged regularly. The B-Spline surface function and autonomous numerical partition algorithm are both applied to describe the instantaneous wetted surface panels. In order to include the influence such as incident wave fluctuation, ship motion, unsteady fluid disturbance and steady ship waves, the instantaneous interception algorithm is also used to re-mesh the wetted surface panel at each time step. In the interception algorithm, the relative position between hull wetted surface panel and free wave surface is summarised as three conditions. This panel classification is further illustrated in Fig.6.

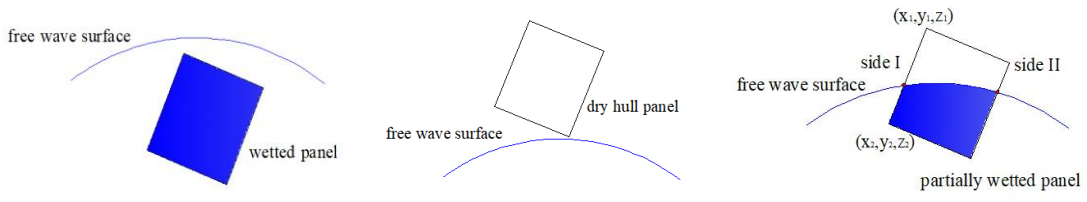

(a) (b) (c)

Fig.6 Instantaneous hull panel generation: (a) wetted panel; (b) dry panel;(c) partially wetted panel

When the hull panel is completely under the free surface, the panel is regarded as a valuable hydrodynamic panel and provide wave pressure fully for the trimaran. If the hull panel is completely above the free wave surface, it is classified as a dry hull panel and is no longer assumed to have any disturbing effect on the fluid. However, for a partially wetted panel, the special interception processing needs to be done. Firstly, it is necessary to find the panel edges (side I and side II) that intersect with the free surface. Subsequently, the

intersection points between the free surface and the panel edges are determined. The point $(x_{\mathrm{I}}, y_{\mathrm{I}}, z_{\mathrm{I}})$ at the panel edge (side I) can be written as:

$$\begin{cases} x_{\mathrm{I}} = \upsilon(x_2 - x_1) + x_1 \\ y_{\mathrm{I}} = \upsilon(y_2 - y_1) + y_1 \\ z_{\mathrm{I}} = \upsilon(z_2 - z_1) + z_1 \end{cases} \tag{41}$$

where υ is the panel slope; (x_1, y_1, z_1) and (x_2, y_2, z_2) are the node locations at the panel edge (side I). The intersection point equation is found by considering the simulated free surface elevation:

$$f(\upsilon) = \zeta_I(x_{\mathrm{I}}, y_{\mathrm{I}}) + \zeta_S(x_{\mathrm{I}}, y_{\mathrm{I}}) + \zeta_D(x_{\mathrm{I}}, y_{\mathrm{I}}) - [\upsilon(z_2 - z_1) + z_1] = 0 \tag{42}$$

The panel slope υ is obtained by using least squares method and iterative calculation, and the intersection point is found. The establishment of intersection points at side II is taken in the same way. These intersection points are finally used to replace the panel nodes to form a new wetted panel. If the new panel is not a complete quadrilateral, the original wetted panel will be decomposed into four small rectangular panels and repeat the panel partitioning steps above. Eventually, all the corrected wetted panels below the fluctuating waterline are generated.

3.2 Convergence analysis

In the time-domain Rankine method, the density of hydrodynamic panels at free surface and hull surface is an important factor in supporting the simulation accuracy. The dimensions of the free surface are fixed. Its range covers the trimaran wetted surface and some additional space for the interference between ships and waves. In the numerical simulation, the length of the free surface quadruple the trimaran length, and its width is 16 times of the trimaran width. By adjusting the mesh size of panels, the panel density of the free surface can be controlled.

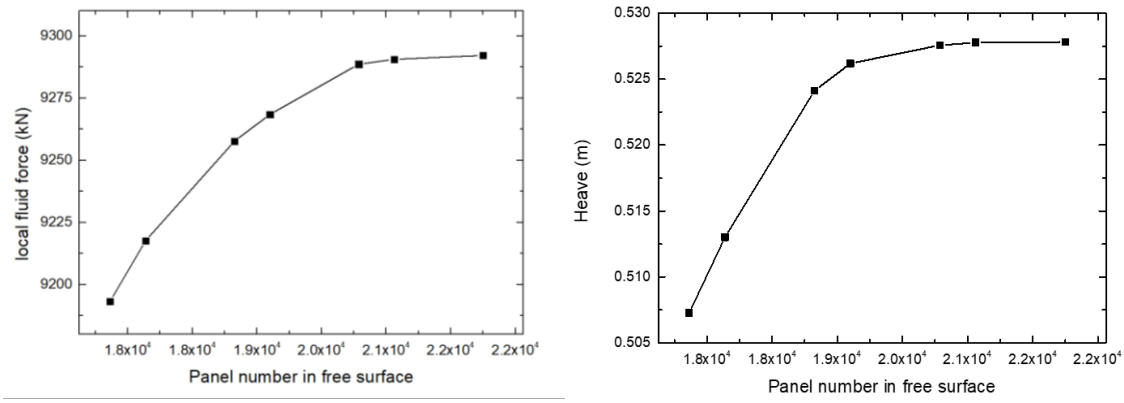

(a) (b)

Fig.7 Relationship between free surface panel number and simulation results (H=1.0m, U=18kn, $\lambda / L = 1.0$): (a) local fluid force; (b) heave

Fig.7 shows the tendency of fluid force and heave with the increasing of panels at the free surface. The numerical simulation of trimaran load and motion converges gradually at higher panel density. When the number of free surface panels reaches 22000, the simulation values for both load and motion become stable. Similar results were also found in the wave cases with different wavelengths. The relative error between the result with the free surface panel number of 22000 and the result with the free surface panel number of 20900 is always less than 0.036% in different ratios of wave length to ship length $(\lambda / L = 0.7, 0.8, 0.9, 1.0, 1.1)$. This free surface panel number (22000) is considered to be enough to predict the trimaran

load and motion. A convergence phenomenon is also found in the meshing of hull surfaces, as shown in Fig.8. The predicted amplitudes of trimaran load and motion will remain relatively stable, when the hull surface panel number exceeds 4620. Similarly, the relative error between the prediction with the hull surface panel number of 4620 and the result with the hull surface panel number of 4200 is found to be lower than 0.025% in different ratios of wave length to ship length $(\lambda / L = 0.7, 0.8, 0.9, 1.0, 1.1)$. This hull surface panel number (4620) also meets the needs of general engineering applications.

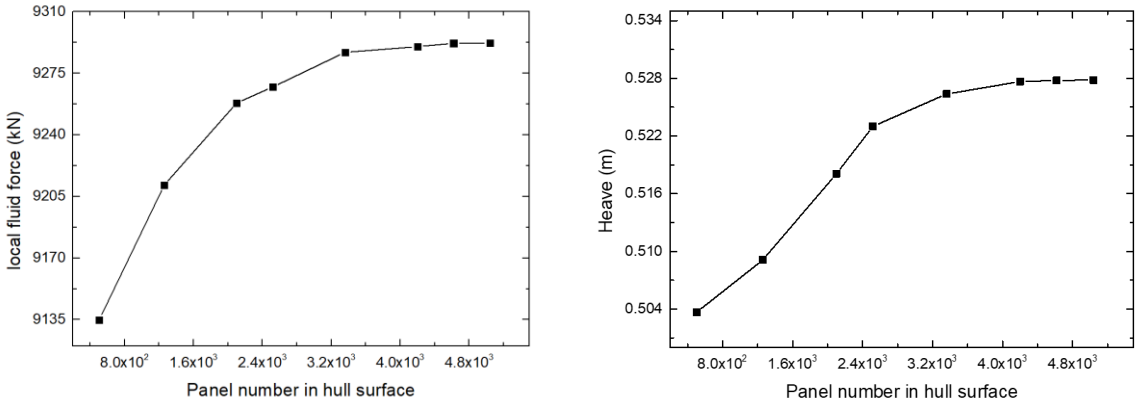

(a) (b)

Fig.8 Relationship between hull surface panel number and simulation results (H=1.0m, U=18kn, $\lambda / L = 1.0$): (a) local fluid force; (b) heave

3.3 Characteristics of instantaneous impact load at trimaran

When a trimaran is sailing in rough seas, it is not difficult to observe the instantaneous impact phenomena of green water and slamming. Although low-frequency wave loads accounts for a large proportion of statistical wave-induced load, the instantaneous impact loads caused by slamming and green water cannot be ignored. Fig. 9(a) shows simulated time histories of slamming at various locations. The time-domain slamming simulation can reflect the fluctuation characteristics well for both the bow and the wet deck. Evidently, when slamming impact occurs, the simulated force rises and reaches a peak rapidly. The slamming force subsequently falls back and disappears after a short period of time. These slamming time-domain characteristics are consistent with monitored fluctuation of slamming pressure in related model experiments [15]. Furthermore, the slamming occurrence time and peak amplitude are found to be varied with different simulated positions. Considering the relatively large acceleration between the wave and the trimaran bow, the slamming at the bow of trimaran main hull always occurs at the earliest time. Additionally, this wave slamming is also the most violent among the three simulated positions. The outrigger slamming at bow is then observed after the main hull slamming. The last wave slamming occurs at the wet deck. In fact, the varied longitudinal distance from the trimaran's gravity centre and the fluid disturbances around these simulated locations are the main reasons for the differences in slamming occurrence times and peak amplitudes. For trimaran slamming loads, the relative acceleration caused by pitch motion always varies in different longitudinal locations. This acceleration influence grows with the longer distance from the ship center of gravity. As the outrigger bow is closer to the ship center of gravity among these simulated locations, the slamming at the outrigger bow occurs relatively late. In addition, the shell of the outrigger bow is sharp and offers only small area for wave impact, which leads to a relatively lower slamming peak. For the wet deck slamming, as the trimaran cross-bridge is arranged at stern, its pitch acceleration is reversed. This reversed acceleration delays the occurrence of wave slamming at the wet deck. Due to the variance of hull shell shape and arrangement along the

longitudinal positions, there are some different disturbances towards the surrounding fluid field. These diverse disturbances always arise the various wave surface fluctuations and aggravate slamming differences further. Considering the large impact area on the trimaran wet deck, its slamming peak amplitude is second only to that of the main hull bow.

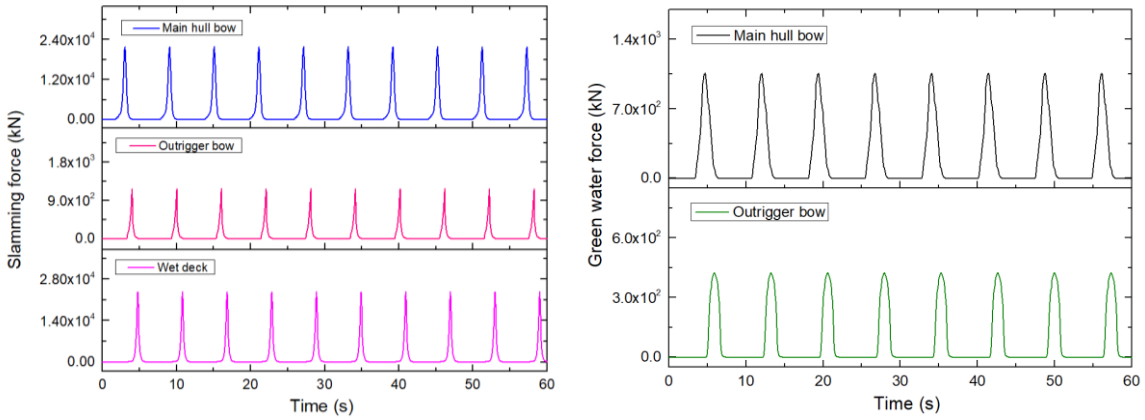

(a) (b)

Fig.9 Simulated time histories of instantaneous load in different locations (H=7.0m, U=18kn, $\lambda / L = 1.0$): (a) slamming force; (b) green water force

The time-domain green water impact is also shown in Fig. 9(b). This green wave force also shows the characteristics of rapid increases and drops, which is similar to the instantaneous slamming fluctuation. But the process of the green water lasts longer and appears weaker steepness in comparison with wave slamming curve. In heading sea, the trimaran main hull collides with the moving wave firstly and generates an initial green water phenomenon. Then, the wave continuously propagates to the outrigger bow and another green water phenomenon appears in the second collision. The green water occurrence time of the outrigger bow is thus much later than that at the main hull bow. Due to the relatively narrow deck space at the outrigger bow, the peak of green water force at the outrigger is also lower than the impact peak at the main hull bow. Considering the fluid interference between the outrigger and the main hull in the trimaran tunnel, the complex wave surface elevation around the outrigger often appears, which also make the fluctuation of green water peak milder.

The fluid fluctuation around the trimaran was simulated in varied wave heights and sailing speeds to observe the fluctuation characteristics of instantaneous impact loads in different wave environments, as shown in Fig.10. When the wave crest propagates near the bow of outrigger in Fig.10(a), the wave surface elevation phenomenon around the outrigger is more evident. The slamming and green water at the outrigger often occur around this moment. With the enlargement of wave height and speed, the trimaran sailing disturbance effect towards the surrounding fluid field increases, as shown in Fig.10(b). When the trimaran is sailing away from one wave trough and forward to another wave crest, the water surface at its main bow rises rapidly. Thus, the slamming and green water occurs at main hull bow. In addition, the wave surface in the tunnel has an obvious elevation effect and contains more high-frequency fluctuations compared with the fluid field around the main hull.

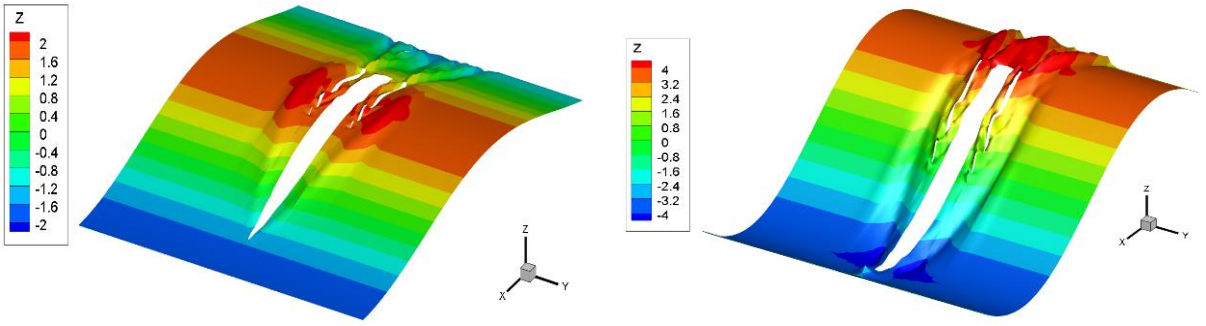

(a) (b)

Fig.10 Simulated fluid fluctuation around trimaran: (a) case I (H=2.0m, U=8kn, $\lambda / L = 1.0$); (b) case II (H=4.0m, U=20kn, $\lambda / L = 1.0$)

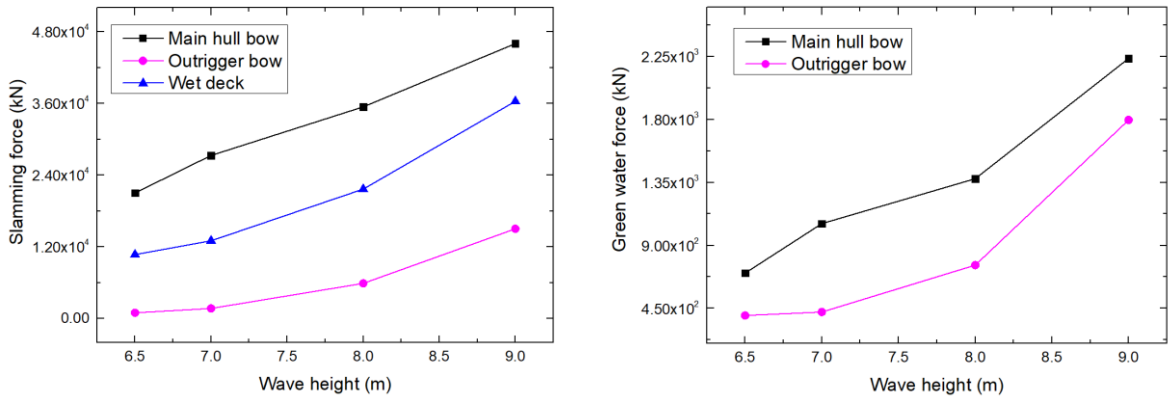

(a) (b)

Fig.11 Instantaneous load in different wave heights (U=8kn, $\lambda / L = 1.0$): (a) slamming force; (b) green water force

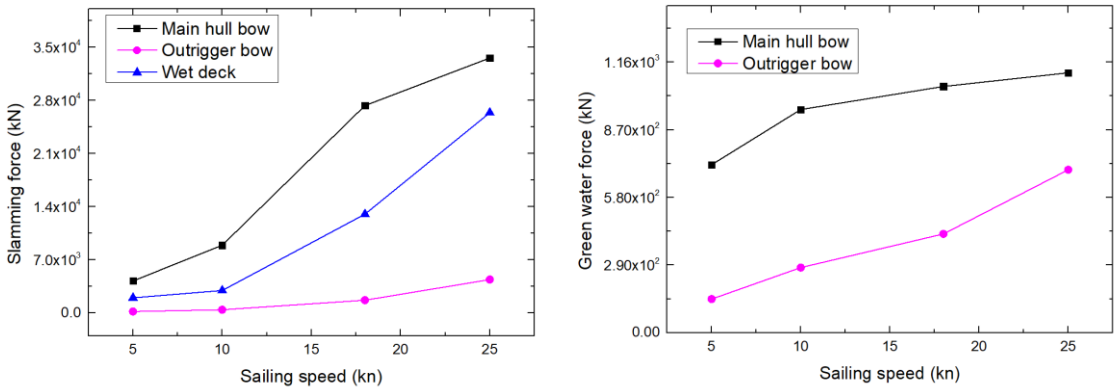

(a) (b)

Fig.12 Instantaneous load in different sailing speeds (H=7m, $\lambda / L = 1.0$): (a) slamming force; (b) green water force

The green water and slamming forces at different wave heights and speeds were counted and analysed. Fig. 11 shows the statistical mean peaks of green water and slamming at various wave heights. Obviously, the slamming became more violent with higher wave height. Furthermore, the mean peak growing trend varies at different positions. Among the simulated positions, it is indicated that wave slamming at the main hull is always largest and has linear growth in different wave heights. However, a nonlinear growth is observed at the statistical peak of the wet deck and the outrigger, as the wave height increases. Due to the mutual disturbance between the outrigger and main hull on the wave surface, the growth rate of the slamming peak at the wet deck and the outrigger is bigger in high wave height cases.

For the green water in different wave heights, the observed growth is similar to the slamming growth. Although the green water impact is relatively weak at the outrigger, its nonlinear increasing trend is still obvious in high wave height cases. Obviously, the wave surface mutual disturbance between the outrigger and main hull cannot be ignored in the trimaran green water phenomenon. The peak tendency of green water and slamming at different sailing speeds was also observed, as shown in Fig.12. It is indicated that the slamming peaks at all three locations grow with the increasing of trimaran sailing speed. The slamming peak growth rate of the wet deck and the outrigger are enlarged at higher speeds, while the increasing trend of slamming peak at the main hull slows down slightly. The speed effect on trimaran tunnel slamming, which includes slamming at the wet deck and the outrigger, is enlarged to a certain extent at higher speeds. In addition, this growth rule in different speed is also suitable for the green water force at the outrigger and the main hull bow. The green water phenomena become more severe with the increasing of sailing speed. Furthermore, the increasing rate of green water force at the outrigger bow is raised obviously in the cases of higher sailing speed. It is suggested that the hydrodynamic force at the outrigger bow is more sensitive to the variation in sailing speed, whether slamming or green water.

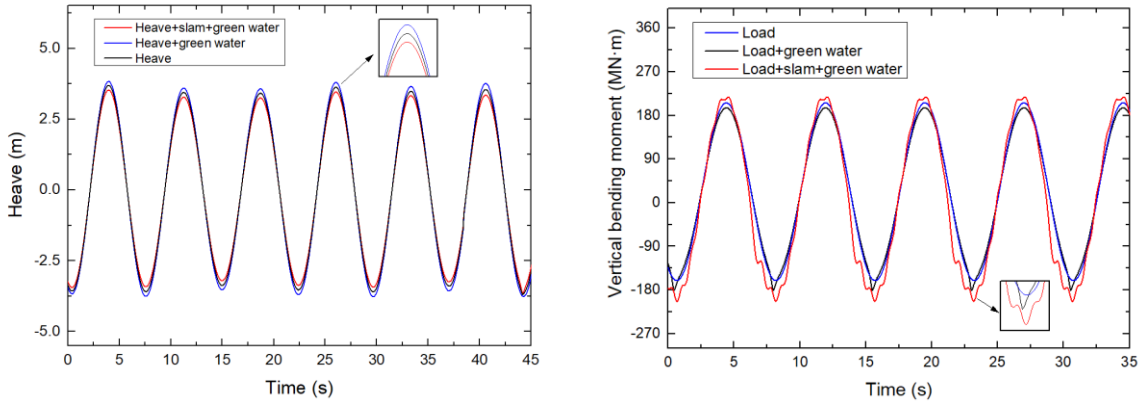

(a) (b)

Fig.13 Influence of instantaneous load for trimaran motion and load (H=8.0m, U=8kn, $\lambda / L = 1.0$): (a) heave motion; (b) midship load

The influence of green water and slamming on trimaran motion and wave-induced load is observed. Fig. 13(a) shows the time histories of trimaran motion after the application of the slamming and the green water. The time-domain motion results without the instantaneous impact and the motion results after only the application of the green water are included in the figure to facilitate the comparison of motion curve characteristics. It is indicated that the simulated trimaran motion become more violent when the green water force is added into the motion simulation. Although the time-domain fluctuation pattern of heave motion does not change obviously, its fluctuation amplitude increases. However, this increased amplitude caused by green water is offset by the influence of wave slamming. The amplitude of heave motion is finally reduced under the combined influence of green water and slamming. This motion weakening phenomenon under the effect of green water and slamming is always found in different cases. The influence of green water and wave slamming towards the trimaran load is also significant. The instantaneous impact of green water and wave slamming leads the load fluctuation curve to become steeper, especially in the trough. It is the superposition result of wave hydrodynamic pressure, slamming pressure, and green water pressure. When the slamming and the green water appear in the simulation, the simulated load will rapidly increase and result in a sudden rising change in the load curve. When the phenomena of slamming and green water finish, this curve protrusion will also disappear. Due to the simulation of slamming and green water at five locations, the load curve shows the multiple

abrupt changes in peak and trough. In addition, the load curve will change overall, due to the changes in trimaran motion under the impact of slamming and green water. The amplitude of vertical bending moment (VBM) amidships increases under the influence of instantaneous wave impact, as shown in Fig. 13(b). Obviously, the characteristics of the trimaran load fluctuation become more complex under the effects of green water and slamming. Therefore, the impact of green water and slamming should be considered in numerical simulation of trimaran load, especially under the conditions of large wave height or high speed.

3.4 Comparative analysis of trimaran load

In order to demonstrate the reliability of the nonlinear time-domain Rankine method on theoretical prediction, the monitored data were extracted from a series of trimaran model tests [15]. Fig. 14 shows the design and implementation process of the model test. The model was connected to a motion monitoring instrument. When the trimaran model sailed in waves, two vertical rods of the motion monitoring instrument moved in unison. The trimaran heave motion was thus monitored by measuring the motion of these vertical rods. As the trimaran model shell was segmented, the longitudinal steel backbone installed in the model would appear bending deformation by uneven wave pressure when the trimaran model was sailing in waves. Some strain monitoring sensors were also installed in the longitudinal steel backbone to measure the fluctuation of surface strain. The calibration test towards the steel backbone was taken before the model test. The relationship between the sectional load and the monitored surface strain is established. Therefore, the fluctuation of the sectional load can be monitored in the model sailing test. The sectional load monitoring location midships was 67.9 m from the fore perpendicular. The monitoring sensors at the bow and stern were at 25.4 m and 107.0 m, respectively, from the fore perpendicular.

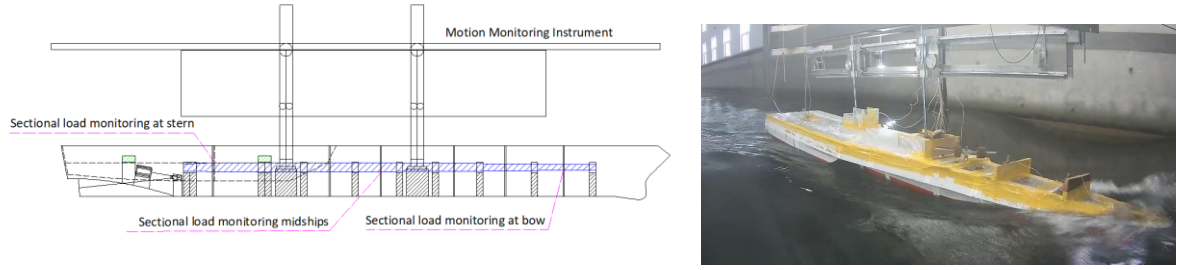

(a) (b)

Fig.14 Description of trimaran model test: (a) trimaran model design and corresponding monitoring instruments; (b) implementation process of trimaran model test

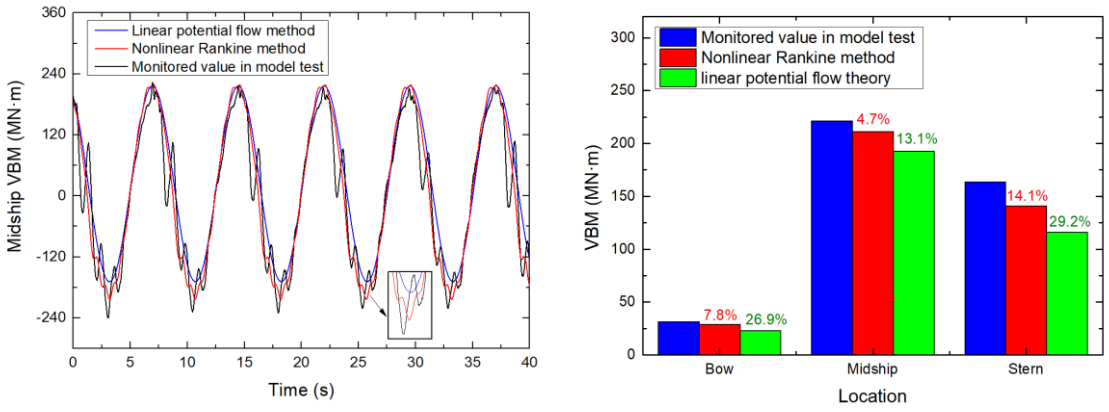

(a) (b)

Fig.15 Comparison of load prediction and experimental values for trimaran (H=8.0m, U=8kn, $\lambda / L = 1.0$): (a) time histories of midship load; (b) load along ship length

The experiment was carried out in a towing tank, 510*m* long, 6.5*m* wide, and 4*m* deep. The distance between the model and wave generator was about 150*m*, and this distance can also be adjusted to suit the changes in model speed. The leading waves at the beginning of wave generation was excluded by a wave monitor, which was placed 25*m* away from the wave maker. A wave dissipation beach, with a slope of 15 degrees, was also arranged at the end of towing tank to eliminate the wave reflection effect [32,33]. The average measurement time for the model tests was about 3 minutes. Slamming and green water at the trimaran bow were observed during the model tests, as seen in Fig. 14(b). Then, a comparative analysis between the theoretical predictions and model tests is taken and shown in Fig. 15. Herein, the traditional linear potential flow method is developed from Sun's research [34]. For the amplitude of wave load fluctuation, the prediction value based on linear potential flow method was always less than the value calculated by the nonlinear Rankine method. The predicted amplitude in the nonlinear Rankine method is closer to the monitored value in the experiment. In addition, the influence of instantaneous impact leads the predicted fluctuation in the nonlinear Rankine method to be more violent and steeper in comparison with that fluctuation in the traditional load forecasting. Some deviation between theoretical prediction and model tests is thus reduced after considering the instantaneous nonlinear factors such as instantaneous wetted surface, steady ship waves, green water and slamming. The deviation between the nonlinear theoretical prediction and the experimental results was analysed further, as shown in Fig. 15 (b). In order to observe the error variation in different wave cases, the relative errors of load prediction caused by linear potential flow theory and nonlinear Rankine method is calculated respectively in the reference of the statistical values in model tests:

$$e_r = \frac{\left|A_m - A_p\right|}{A_m} \times 100\% \tag{43}$$

where e_r denotes the trimaran load relative error between the theoretical prediction and model tests; A_m is the statistical load amplitude in model test; and A_p is the simulated amplitude of the theoretical prediction using the nonlinear Rankine method or linear potential flow method. The relative errors of the load predictions by each method are marked at the top of histogram. It is indicated that the relative error of load prediction amidships in the nonlinear Rankine method is 8.4% less than that prediction in the traditional linear potential flow method. In the comparison between the nonlinear Rankine method and the linear potential flow method, an improvement of the theoretical prediction accuracy in the nonlinear Rankine method is also found at bow and stern. However, at all longitudinal monitoring positions, the experimental value is still larger than the load predictions. Furthermore, the relative errors grow obviously at bow and stern. In the nonlinear Rankine method, the bow relative error increases by 3.1%, and the stern relative error increases by 9.4%. There are many reasons for these deviations. Firstly, the wave propagation is always influenced by fluid viscosity. The real waveform will change, when the waves touch the trimaran shell. Moreover, the wave will break further under the collision between hulls and waves during some high-speed cases. The wave breaking process always varies with speed, ship shell, waveform, and wave height. In addition, the complex flow disturbance and extra vibration caused by the stern propeller also make the actual measured values in the model deviate from the theoretical predicted values. Therefore, the stern is also found as the position with the greatest deviation for trimaran load simulation. Although the load prediction based on the nonlinear Rankine method still deviates slightly from the experimental values, this method can predict the load fluctuations of the trimaran relatively accurately under the combined action of green water and slamming. For the trimaran load prediction, it is thus superior to the traditional linear potential flow prediction method.

In the ship structural longitudinal strength assessment, the wave condition where the wavelength is close to the ship length is usually considered to be dangerous [35]. Therefore, a series of simulations towards the trimaran load are taken, when the ratio of wavelength to ship length (λ / L) approaches 1.0. The theoretical load prediction and experimental values amidships under different sailing speeds and ratios of wavelength to ship length were then summarized to analyse the distribution characteristics of the trimaran load. The relative errors are also marked at the top of the statistical histogram. Fig. 16(a) shows that the vertical bending moment amidships from both the theoretical prediction and model experiment has obvious growth as the wave height increases. It is indicated that the experimental monitored value has the highest growth rate. When the wave length-ship length ratio is 0.7, the wave load amidships in medium wave height is overestimated by both the linear potential flow method and the nonlinear Rankine method. However, when the wave height is raised to 8 m, the experimental value grows obviously and is higher than the theoretical prediction by either numerical method. The maximum vertical bending deformation occurs when the ratio of wave length to ship length is 0.9. It is indicated that this load distribution is relatively stable in different wave height cases. Furthermore, the simulated loads by the two prediction methods always remain lower than experimental load response at the maximum load distribution position. When the wave height is at 4 m, the relative error between the experimental value in model test and the load prediction in the linear potential flow method is 11.5%. However, the relative error for the nonlinear Rankine method is 4.0%. The relative error increases by only 0.7% in this Rankine method, when the wave height is continuously raised to 6 m. Thus, although the relative error does grow as the wave heights increases, the Rankine prediction under considering the effect of instantaneous load impact still remains closer to the real value derived from the model test.

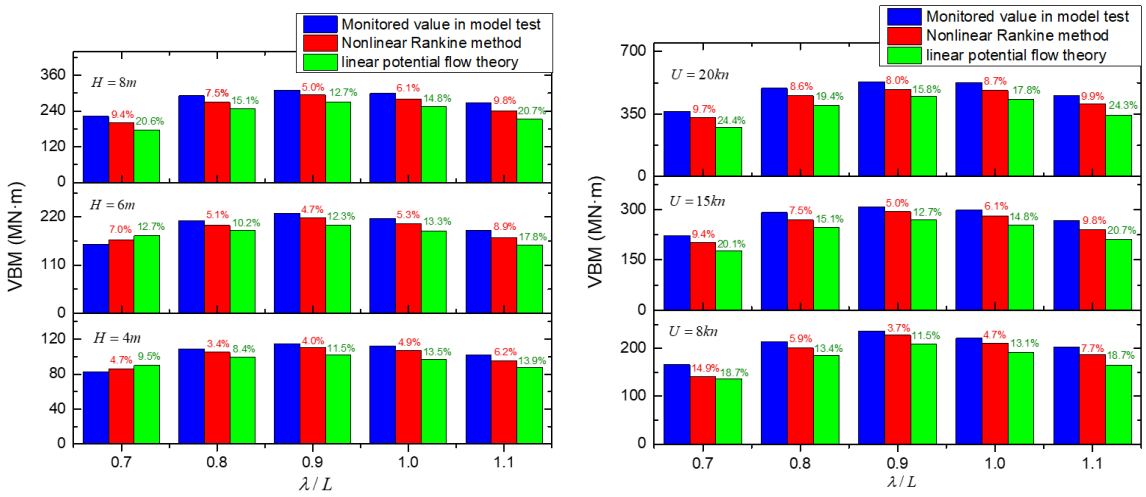

(a) (b)

Fig.16 Statistics of load prediction and experimental values for trimaran amidships: (a) statistical results at different wave heights (U=15kn); (b) statistical results at different sailing speeds (H=8.0m).

The same ratio of wavelength to ship length ($\lambda / L = 0.9$) is confirmed to be the most violent load conditions for various sailing speeds, as seen in Fig. 16 (b). The pattern of load distribution at various speeds is similar to the distribution at different wave heights. In the comparative analysis, it is found that the Rankine prediction method is better than the liner potential flow method although its simulated values still remain lower than the experimental values. The relative error for the nonlinear Rankine method grows from 3.7% to 8.0%, when the sailing speed increases from 8kn to 20kn. In the comparison with the deviation of load prediction in various wave heights, the fluctuation of load prediction deviation caused by different speeds is more evident. It is indicated that sailing speed is more relevant to the load

deviation between the theoretical prediction and the experimental value. In general, the deviation of the nonlinear Rankine method remains consistently lower than that of the linear potential flow method for variations in both wave height and sailing speed. The nonlinear Rankine method thus becomes more suitable for trimaran load prediction, especially for large wave heights and high sailing speeds. In addition, as the nonlinear Rankine method is relatively simple and flexible in implementation of numerical simulations, it is recommended for application in both preliminary hull shell design and structural strength assessments for trimarans.

4. Conclusions

For the load prediction of trimarans, a kind of time-domain weakly nonlinear Rankine method was developed, which accounts for the influence of instantaneous hull wetted surface, steady ship waves, green wave and slamming. The good numerical convergence in this Rankine method is achieved by using the techniques such as damping layer and numerical filtering. Finally, the comparative analysis is taken to verify the accuracy of trimaran load prediction. Correlative conclusions were thus derived as follows:

(1) The time correlation between low-frequency wave load and instantaneous wave impact is well reflected in the nonlinear Rankine method. Unlike the simple superposition of linear hydrodynamic force and instantaneous wave impact components, the nonlinear Rankine method adds green water and slamming force into the solution of ship motion equation and takes the influence of steady ship waves into account in all hydrodynamic simulations. Thus, the simulated load can take full consideration of the time-domain relationship between wave propagation and hull motion.

(2) The nonlinear increasing of green water and slamming is observed at the wet deck and the outrigger, with the growth of sailing speed and wave height. In high sailing speed or wave height cases, the fluid interference between the outrigger and main hull will enlarge the instantaneous wave impact and cause this nonlinear load growth.

(3) The accuracy of theoretical prediction towards trimaran load is improved by using the time-domain nonlinear Rankine method. This Rankine method can accurately describe the trimaran load distribution in different wavelengths and offer relatively accurate predicted values. Some sudden fluctuations caused by the instantaneous wave impact are also predicted in the load curve. Additionally, the theoretical prediction amidships in the nonlinear Rankine method is more accurate than the forecast at bow and stern. It is feasible to apply this predicted value to verify the reliability of longitudinal structure strength amidships.

In this research, the weakly nonlinear Rankine method is effective under the influence of instantaneous hull wetted surface, steady ship waves, green wave and slamming. However, some factors were still ignored in the development of the numerical model, which may explain some deviation from experimental results. Future research should pay more attention to fluid viscosity. And the factors such as wind load and air cushions in the tunnel should also be included to improve the theoretical prediction accuracy for trimaran load in harsh marine environments.

ACKNOWLEDGMENTS

This research was supported by the National Natural Science Foundation of China (No. 52201353), the Natural Science Foundation of Liaoning Province (No.2021-BS-078 and No. LJKZ0046). And all authors express their gratitude to these foundations.

REFERENCES

[1] Burak, Y., 2022. Prediction of residual resistance of a trimaran vessel by using an artificial neural network. *Brodogradnja*, 73(1), 127-140. https://doi.org/10.21278/brod73107

[2] Noblesse, F., 1983. Integral identities of potential theory of radiation and diffraction of regular water waves by a body. *Journal of Engineering Mathematics*, 17(1), 1-13. https://doi.org/10.1007/BF00042834

[3] Ozdemir, Y. H., Cosgun, T., Barlas B., 2021. Wave field generated by finite-span hydrofoils operating beneath a free surface. *Brodogradnja*, 72(1), 145-167. https://doi.org/10.21278/brod72108

[4] Telste, J. G., 1986. Noblesse, F. Numerical evaluation of the green function of water-wave radiation and diffraction. *Journal of Ship Research*, 30, 69-84. https://doi.org/10.5957/jsr.1986.30.2.69

[5] Lu, X. P., Li, Y. Dong, Z. S., 2005. A research summary on high speed trimaran, *Journal of Naval University of Engineering*, 17(2), 43-44.

[6] Kim, Y. H., Kring, D. C., Sclavounos, P. D., 1997. Linear and nonlinear interaction of surface waves with bodies by a three-dimensional Rankine panel method. *Applied Ocean Research*, 19(5), 235-249. https://doi.org/10.1016/S0141-1187(97)00034-5

[7] Shin, Y. S., Belenky, V. L., Lin, W. M., Weems, K. M., Engle, A. H., 2003. Nonlinear time domain simulation technology for seakeeping and wave-load analysis for modern ship design, *Transactions*, 111, 557-583.

[8] Xiang, J. Y., Mao, X. F., 2008. Hull variation based on the main hull parameters. *Chinses Journal of Ship Research*, 3, 15-18.

[9] Xu, W., 2008. Study on numerical calculation of wave-induced motions and loads for trimaran. Master thesis, *Shanghai Jiao Tong University*, Shanghai, China.

[10] Deng, Q., Mao, X. F., Wu M. H., 2016. Effect of principal dimensions on seakeeping and wave loads of trimarans, *Chinese Journal of Ship Research*, 11(6), 8-14.

[11] Tang, H.Y, Zhang, X. K., Ren, H. L., Yu, P. Y., 2020. Numerical study of trimaran motion and wave load prediction based on time-domain rankine-green matching method. *Ocean Engineering*, 214(2), 107605. https://doi.org/10.1016/j.oceaneng.2020.107605

[12] Khoob, A. A., Ketabdari, M. J., 2020. Short-term prediction and analysis of wave-induced motion and load responses of a wave-piercing trimaran. *Brodogradnja*, 71(2), 123-142. https://doi.org/10.21278/brod71208

[13] Tang, H. Y., Ren, H. L., Zhong, Q., 2019. Design and model test of structural monitoring and assessment system for trimaran. *Brodogradnja*, 70(2), 111-134. https://doi.org/10.21278/brod70206

[14] Nowruzi, L., Enshaei, H., Lavroff, J., Davis, M. R., 2020. Parametric study of seakeeping of a trimaran in regular oblique waves. *Ships and Offshore Structures*, 15, 1-12. https://doi.org/10.1080/17445302.2020.1735809

[15] Tang, H. Y., Ren, H. L., Wan, Q., 2017. Investigation of longitudinal vibrations and slamming of a trimaran in regular waves, *Journal of Ship Research*, 61(3), 53-166. https://doi.org/10.5957/JOSR.170001

[16] Chen, X., Zhu, R. C., Zhao, J., 2018. Study on weakly nonlinear motions of ship advancing in waves and influences of steady ship wave. *Ocean Engineering*, 150, 243-257. https://doi.org/10.1016/j.oceaneng.2017.12.053

[17] Kring, D.C., 1994. Time domain ship motion by a three-dimensional Rankine panel method. PhD Thesis, *MIT*, Cambridge, UK.

[18] Wang, W.F., 2010. Time domain 3D wave loads calculation of ships with forward speed based on Rankine panel method. Master thesis, *Harbin Engineering University*, Harbin, China.

[19] Li, X.L., 2014. Comprehensive study of wave induced load and structural strength analysis of trimaran. Master thesis, *Shanghai Jiao Tong University*, Shanghai, China.

[20] Shao, Y., 2010. Numerical potential-flow studies on weakly-nonlinear wave-body interactions with/without small forward speeds. PhD thesis, *Norwegian University of Science and Technology*, Trondheim, Norway.

[21] Liu, Y., Miao,G., 1986. Theory of Ship Motions in Waves. *Shanghai Jiao Tong University Press*, 41-49.

[22] Wang, J.L., 2010. Calculating the dynamic response of high-speed catamarans in head waves. Master thesis, *Tianjin University*, Tianjin, China.

[23] Liapis, S.J., Beck, R.F., 1985. Seakeeping computations using time-domain analysis, *Proceedings of the 4th International Symposium on Numerical Hydrodynamics*, USA.

[24] Sun, W., 2015. Three dimensional time domain numerical method for large amplitude ship motions. PhD thesis, *Harbin Engineering University*, Harbin, China.

[25] Tang, K., 2014. Time domain hybrid green function method and prediction of ship motions in waves. PhD thesis, *Shanghai Jiao Tong University*, Shanghai, China.

[26] Hess, J. L., Smith, A. M. O., 1964. Calculation of non-lifting potential flow about arbitrary three-dimensional bodies. *Journal of Ship Research*, 8, 22-44. https://doi.org/10.5957/jsr.1964.8.4.22

[27] Longuet-Higgins, M. S., Cokelet, E., 1976. Deformation of steep surface waves on water. I.A numerical method of computation. *Proceedings of the Royal Society of London A: Mathematical, Physical and Engineering Sciences*, London, England.

[28] Zhang, K.H., 2018. Research on nonlinear wave loads' time-domain hydroelastic analysis method and application of ships with large bow flare. PhD thesis, *Harbin Engineering University*, Harbin, China.

[29] Buchner, B., Cozijn, J. L., 1997. An investigation into the numerical simulation of green water, In *Proceedings of the Eighth International Conference on the Behaviour of offshore structures*, BOSS'97, Oxford, England.

[30] Jiao, J. L., Yu, H. C., Chen, C. H., Ren, H. L., 2019. Time-domain numerical and segmented model experimental study on ship hydroelastic responses and whipping loads in harsh irregular seaways. *Ocean Engineering*, 185, 59-81. https://doi.org/10.1016/j.oceaneng.2019.05.039

[31] Chen, Z.Y., Ren, H. L., Zhang, K. L., 2012. Experimental and numerical analysis of bow slamming and whipping in different sea states. *Journal of Ship Mechanics*, 16(3), 246-253.

[32] Ismail, M. A., Shaharuddin, N. M. R., Yaakob, O., Jamal, M. H., Adnan, F. A., Rashidi, A. H. M., Azhary, W. A. H. W. M., Samion, M. K. H., Bachok, A., Ahmad, B., Ahmad, N. S. 2022. Wake wash of a fast small boat in restricted waters: model tests and full-scale measurements. *Brodogradnja*, 73(2), 93-119. https://doi.org/10.21278/brod73206

[33] Tang, H. Y., Ren, H. L., Yu, P. Y., Tian, B. J., 2020. Experimental investigation of seakeeping performance and load response of trimaran in small heeling condition. *Applied Ocean Research*, 101, 102275. https://doi.org/10.1016/j.apor.2020.102275

[34] Sun W.; Ren, H. L., Li, H., Wang, C., 2014. Numerical solution for ship with forward speed based on transient Green function method. *Journal of Ship Mechanics*, 18(12), 1444-1452.

[35] Wang, X. Z., Liu, J. H., 2020. Analysis of global loads characteristics and strength of a trimaran, *Naval architecture and ocean engineering*, 36(6), 19-23.

Submitted: 05.04.2023.
Accepted: 27.06.2023.

Haoyun Tang, conanthy@126.com
Navigation College, Dalian Maritime University, No.1 Linghai Road,
High tech Zone, Dalian City, Liaoning Province, China
Qian Wan
Dalian Shipbuilding Industry Company, No. 1, Haifang Road,
Xigang District, Dalian City, Liaoning Province, China
Huilong Ren
College of Shipbuilding Engineering, Harbin Engineering University,
No.145, Nantong Street, Harbin, China